Nano Research
2023, 16(4): 4793–4802

ISSN 1998-0124 CN 11-5974/O4
https://doi.org/10.1007/s12274-022-5261-y

Research Article

CNTs/CNF-supported multi-active components as highly efficient bifunctional oxygen electrocatalysts and their applications in zinc-air batteries

Weiyuan Ding[1,2], Ali Saad[1], Yuchen Wu[1,2], Zhiwei Wang[1,2], and Xiuting Li[1] (✉)

[1] *Institute for Advanced Study, Shenzhen University, Shenzhen 518060, China*
[2] *College of Physics and Optoelectronic Engineering, Shenzhen University, Shenzhen 518060, China*

Received: 28 September 2022 / **Revised:** 26 October 2022 / **Accepted:** 30 October 2022

ABSTRACT

Rational construction of active components has been the biggest challenge in preparing efficient bifunctional oxygen electrocatalysts. Herein, electrospinning and chemical vapor deposition (CVD) were employed to embed active species including FeCo nanoparticles, MN*x* (M = Fe, Co), and FeP*x* in porous and graphitized carbon nanotubes (CNTs)/carbon nanofiber (CNF). The as-prepared FeCo@CoN*x*@FeP*x*/C exhibited a half-wave potential as high as 0.86 V in oxygen reduction reaction (ORR) and low oxygen evolution reaction (OER) overpotential of 368 mV at 10 mA·cm^{-2}, which are superior to Pt/C (0.83 V) and IrO_2 (375 mV) respectively. The assembled Zn-air battery (ZAB) showed a high energy efficiency ($E_{discharge}/E_{charge}$) of 65% at 20 mA·cm^{-2} and stabilized for 700 charge–discharge cycles. The spectroscopic and microscopic characterizations evidenced that the outstanding bifunctionality of the electrocatalyst can be ascribed to three main reasons: First, FeCo nanoparticles are rich in MOH/MOOH active sites for OER, and FeP*x*/CNTs constructed with CVD also modulate electronic structure to improve electron transfer; second, both MN*x* in carbon matrix and FeP*x*/CNTs are highly active towards ORR; third, the CNTs/CNF are highly porous and graphitized, which promotes mass transport and improves electrical conductivity and stability of the electrocatalysts. This work gives important implications on the design of bifunctional electrocatalysts.

KEYWORDS

carbon nanotubes (CNTs)/carbon nanofiber (CNF)-supported, multi-active components, oxygen reduction reaction, oxygen evolution reaction, zinc-air battery

1 Introduction

Nowadays the energy shortage and climate change problems trigger an urgent demand in accelerating the commercialization of clean energy including the fuel cells and metal-air batteries, both of which require highly efficient oxygen electrocatalysts [1–3]. Until now, the most efficient electrocatalysts for oxygen evolution reaction (OER) and oxygen reduction reaction (ORR) are Ir/Ru and Pt-based materials respectively [4–6]. However, the high cost, low abundance, and poor stability of such noble metal materials hamper their commercial application [7]. In addition, lack of multifunctionality is also an obvious disadvantage for the development of those electrocatalysts in clean and sustainable energy devices [8, 9]. Recent studies revealed that constructing particular active components for OER and ORR in carbon matrix is an effective way to prepare bifunctional electrocatalysts with low cost, high activity, and stability [10–12].

In recent years, transition metal alloys (FeCo, CoNi, and FeNi) have received extensive attention due to their outstanding performance as electrocatalyst in clean energy conversion processes [13–17]. Encapsulation of metal alloys into nitrogen-doped carbon materials has been considered as a promising strategy to improve activity and stability, especially for OER electrocatalysis [18–24]. This is because metal–OOH bonds are more likely to be formed on the alloy surface, which was verified to be a typical OER active site. On the other hand, the formation of MN*x* on the nitrogen-doped carbon matrix would promote its ORR activity, because the metal–heteroatom bonds could lower the binding energies of the intermediates *OOH and *OH in ORR [23–25]. In addition, transition metal phosphides have recently been validated as effective ORR/OER active species [4, 16, 23, 24]. However, constructing active sites to achieve highly efficient OER/ORR bifunctionality is still challenging [26–32]. Gao et al. [23] built a new composite catalyst (CoFeP@C) by embedding CoFeP nanoparticles in N, P double-doped carbon matrix. Lu et al. [16] designed five bimetallic phosphide catalysts M-Co_2P@M-N-C (M = Fe, Ni, Mn, AI, Mo), which contain the active substances including bimetallic bonds, metal phosphide, nitrogen-doped carbon, etc. The activity of the above electrocatalysts is still inferior to that of noble metal catalysts, which is likely due to their simple carbon matrix structure with low porosity and hence the exposure of active sites is limited.

In this work, a simple and effective strategy is designed to successively anchor alloy nanoparticles and their metal compounds on high-defect and porous carbon substrate for preparing a highly active and durable bifunctional electrocatalyst. Preparing multi-dimensional carbon fiber via electrospinning has

Address correspondence to xiuting.li@szu.edu.cn

become a popular way to obtain the excellent carbon substrate for loading electrocatalytic active species. The resultant carbon substrate with fiber network has high porosity and large surface area to promote the mass transport in electrocatalysis [33–35]. Chemical vapor deposition (CVD) technology has been proved to be an effective way for constructing active components on electrocatalysts and is increasingly popular in recent studies [36–38]. Thus, we adopted the electrospinning and CVD techniques to construct multiple active species on defect-rich and porous carbon substrate by fully taking the advantages of the spacing effects of the carbon nanofiber. To be specific, a small amount of (0.3 wt.%) Fe and Co ions was first well dispersed in the spinning precursor. By applying high positive and negative voltages (20 and −1 kV) to the precursor, the nanofiber network was formed. After heat treatment, the carbon fiber substrate with highly graphitized and defect-rich structure was obtained and the FeCo alloy nanoparticles were simultaneously embedded. Next, the carbon fiber was successively treated with NH_3 and PH_3 vapor via CVD method under 800 °C. The high-defect and graphited carbon resulted in the maximum exposure of the FeCo alloy nanoparticle, leading to partial conversion of FeCo alloys to MN*x* species and FeP_4 nanoparticles. As a result, the FeCo@CoN*x*@FeP*x*/C nanofiber electrocatalyst with rich porosity and high utilization of active sites was obtained. The half-wave potential of the electrocatalyst reached as high as 0.86 V in ORR, and an overpotential of 368 mV at 10 mA·cm^{-2} in OER, which is superior to both the noble metal catalysts Pt/C (0.83 V) and IrO_2 (375 mV) respectively. Moreover, the assembled Zn-air battery (ZAB) showed a low voltage gap (ΔE) of 0.69 V at 20 mA·cm^{-2} corresponding to a round-trip efficiency ($E_{discharge}/E_{charge}$) of 65% and stabilized for 700 charge–discharge cycles. Therefore, the present strategy provides important implications for developing efficient and stable bifunctional electrocatalysts for applications in clean energy devices such as fuel cells, metal-air batteries, and water splitting.

2 Experimental

2.1 Materials

All reagents were obtained from commercial sources and used as received without further purification. Ferric nitrate nonahydrate, copper nitrate hexahydrate, ethanol, polyvinylpyrrolidone (PVP, K88-K96), Nafion D-521 dispersion, and potassium hydroxide were all purchased from Aladdin (China). N,N-Dimethylformamide (DMF, 99.5%) was obtained from Macleans. Commercial Pt/C (20 wt.% Pt) and IrO_2 were from Suzhou Sinero Technology Co., Ltd. All solutions were prepared using ultrapure water at a resistivity of 18.2 MΩ·cm at 298 K (KMD-SHZ, CD Haochun Inc., China).

2.2 Synthesis of FeCo/C

1 mmol $Fe(NO_3)_3·9H_2O$ and 0.5 mmol $Co(NO_3)_2·6H_2O$ were added into 25 mL DMF solution and stirred on a magnetic stirrer. After dissolved, 3 g of PVP was introduced and stirred for 48 h to ensure that the metal ions were evenly dispersed in the solution. The prepared solution was added into a 10 mL syringe and a 19-gauge needle was employed for electrospinning. The positive and negative voltages used for spinning were 20 and 1 kV respectively, the spinning speed was 0.8 mL·h^{-1}, the running speed of the roller was 300 rap·min^{-1}, the relative humidity of the air was 20%–30%, and the temperature was 25–30 °C. The FeCo composite fiber prepared by electrospinning was dried in a vacuum at 120 °C for 6 h. After drying, the samples were put in a corundum crucible and heated at 800 °C for 2 h in a tube furnace with NH_3 flow. The heating rate was 2 °C·min^{-1}. The FeCo/C sample was then obtained.

2.3 Synthesis of FeCo@MN*x*/C

The FeCo/C catalyst and dicyandiamide ($C_2H_4N_4$) with a mass ratio of 1:4 were placed in the same crucible and a N_2 atmosphere was kept for CVD. Given that the operation with $C_2H_4N_4$ is more convenient and safer than NH_3, $C_2H_4N_4$ was used as the nitrogen precursor. During the vapor deposition, the temperature reached first up to 300 °C at a rate of 5 °C·min^{-1}, and then to 1,000 °C at 2 °C·min^{-1}. The temperature of 1,000 °C was kept for 1 h and dropped to 300 °C at a rate of 7 °C·min^{-1}. The sample was then taken out and naturally cooled down to room temperature. The as-obtained sample was named as FeCo@MN*x*/C.

2.4 Synthesis of FeCo@CoN*x*@FeP*x*/C

The FeCo@MN*x*/C catalyst and NaH_2PO_2 were placed in two separate small crucibles, and CVD was carried out in a N_2 atmosphere. The samples were heated to 400 °C at a rate of 2 °C·min^{-1} and stayed for 2 h. Then it was naturally cooled down to room temperature. The FeCo@CoN*x*@FeP*x*/C was finally obtained.

2.5 Synthesis of other catalysts

The similar preparation procedure was used for synthesising Fe/C, FeN*x*/C, FeN*x*@FeP*x*/C, Co/C, CoN*x*/C, and CoN*x*@FeP*x*/C only without the introduction of $Co(NO_3)_2·6H_2O$ or $Fe(NO_3)_3·9H_2O$. The FeCo@FeP*x*/C was prepared by using FeCo/C catalyst and NaH_2PO_2. The FeCo@MNx^2/C was prepared via twice vapor deposition with $C_2H_4N_4$.

2.6 Material characterizations

The morphology of the electrocatalysts was examined by a field emission Transmission Electron Microscope (JEOL F200). The element distribution was characterized with an energy spectrum analyzer. The nitrogen absorption and desorption curves were obtained on a Brunauer–Emmett–Teller (BET) analyzer (ASAP 2460). The crystal structures were analyzed by high-resolution X-ray diffractometer under Cu Kα radiation between 5°–90°. The structure of the carbon support was characterized by laser micro confocal Raman spectrometer (excitation wavelength: 532 nm, spectral range: 100–8,000 cm^{-1}). The elemental information was provided with X-ray photoelectron spectrometer (Thermo ESCALAB 250XI). The atomic structure of the catalyst was analyzed by using synchrotron radiation hard X-ray (Singapore Light Source). The content of Fe and Co elements in the samples was determined by inductively coupled plasma-optical emission spectrometry (ICP-OES, Agilent 7700). The X-ray absorption spectroscopy (XAS) data analysis, the detailed procedure of electrochemical measurements, and the assembly process of Zn-air battery can be seen in the Electronic Supplementary Material (ESM).

3 Results and discussion

3.1 Catalyst synthesis and characterization

Figure 1(a) illustrates the synthetic process of FeCo/C, FeCO@MN*x*/C, and FeCo@CoN*x*@FeP*x*/C. The morphology of the FeCo/C, FeCo@MN*x*/C, and FeCo@CoN*x*@FeP*x*/C samples was first characterized by transmission electron microscopy (TEM). As for the FeCo/C, it can be observed from Fig. S1(a) in the ESM that the nanoparticles with about tens of nanometer in size are uniformly distributed on the surface of porous carbon fibers. The crystalline spacing in the high-resolution TEM

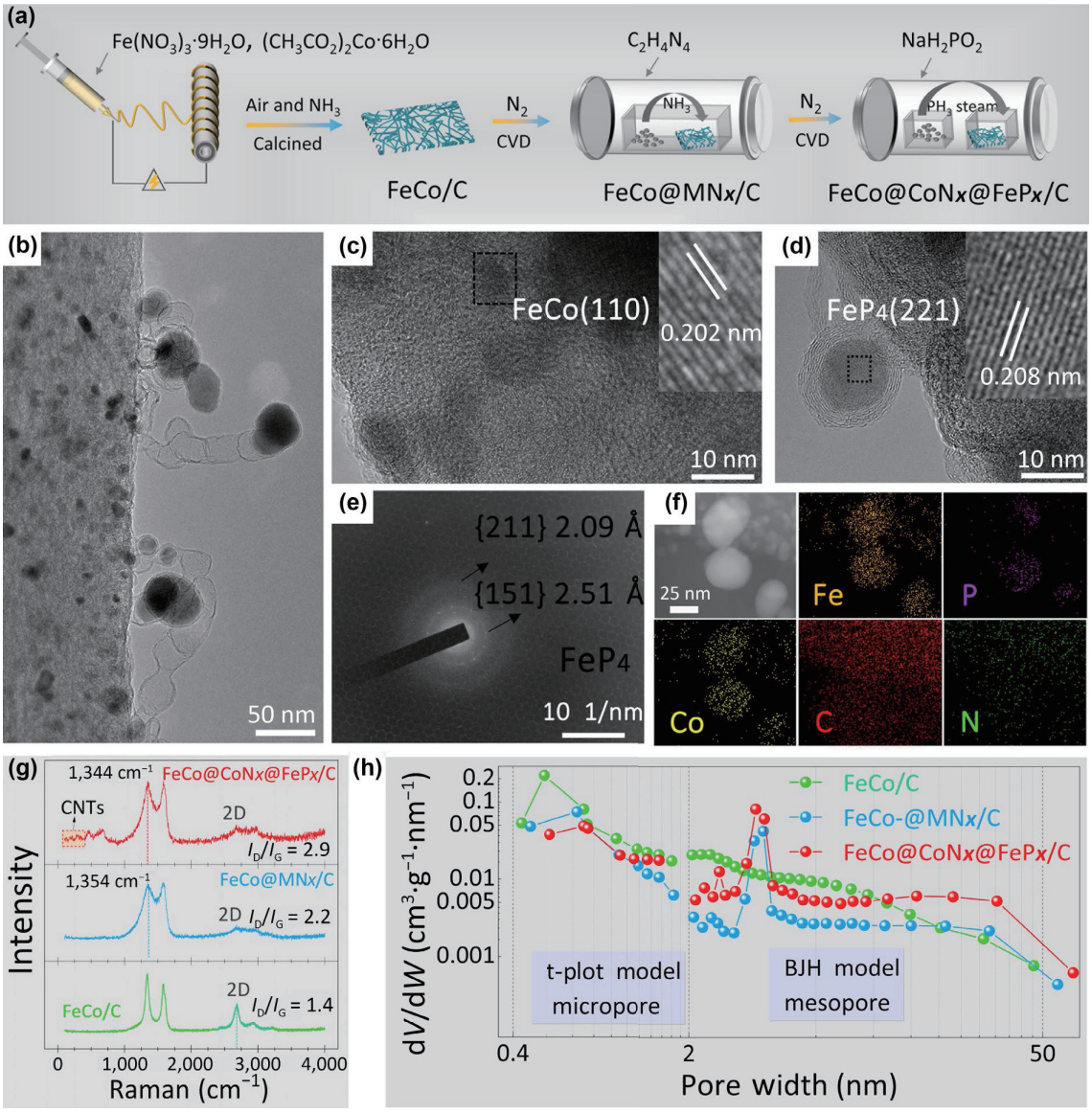

Figure 1 (a) A scheme illustrating the preparation procedure of the FeCo/C, FeCo@MN*x*/C, and FeCo@CoN*x*@FeP*x*/C electrocatalysts. (b) A typical TEM image of the FeCo@CoN*x*@FeP*x*/C fiber. (c) A zoom-in TEM image showing FeCo alloy nanoparticles on the fiber surface. (d) A TEM image of the FeP_4 "head" of carbon nanotube. (e) The diffraction image of FeP_4. (f) The EDS mapping of the FeCo@CoN*x*@FeP*x*/C electrocatalyst. (g) Raman and (h) BET analysis of the three electrocatalyst.

(HRTEM) image (Fig. S1(b) in the ESM) agrees with the (110) plane of FeCo, indicating the successful embedding of FeCo alloys in the carbon substrate via the electrospinning technique. In addition, the FeCo nanoparticles are found to be covered by the multilayers of graphene, which could likely improve the conductivity and stability of the electrocatalysts [39–41]. After the CVD of nitrogen, there is no obvious change in the fiber morphology, as shown in Fig. S2 in the ESM. The typical TEM image of the further phosphatization product FeCo@CoN*x*@FeP*x*/C is shown in Figs. 1(b)–1(e). The FeCo alloy nanoparticles (Fig. 1(c)) and the surface graphene (Fig. 1(d)) remain in the FeCo@CoN*x*@FeP*x*/C fibers. In addition, plenty of carbon nanotubes (CNTs) with a nano-spherical "head" (around 20–40 nm) randomly grew on the fiber surface (Fig. 1(b) and Fig. S3(a) in the ESM). The crystalline spacing of the CNT heads (Fig. 1(d)) agrees with the (221) plane of FeP_4 and both the (151) plane and (221) plane of FeP_4 are evidenced in the diffraction image, demonstrating that the mushroom heads consist of FeP*x*. The hierarchical carbon substrate consisting of CNTs/carbon fiber could stabilize its active sites and increase the conductivity to accelerate the catalytic process. The growth of FeP*x*/CNTs on the fiber surface could not only enable the maximum exposure of active sites but also facilitate the electron transfer kinetics [7]. Energy dispersive X-ray spectroscopy (EDS) mapping (Fig. 1(f) and Fig. S3(b) in the ESM) further evidences the presence of the iron, cobalt, nitrogen, and phosphorus elements in FeCo@CoN*x*@FeP*x*/C. X-ray diffraction analysis (XRD) of the FeCo/C, FeCo@MN*x*/C, and FeCo@CoN*x*@FeP*x*/C catalysts was conducted and the results are shown in Figs. S4(a)–S4(c) in the ESM. The diffraction pattern of all samples shows the (110), (200), and (211) planes of FeCo alloys (00-049-1567) and the graphite (002) plane at 26°. The relative intensity of the later increases after CVD doping, indicating that the degree of graphitization gets higher. Compared with the FeCo/C, the patterns of FeN*x* (FeN_4 and $FeN_{0.088}$) and FeP_4 are found in the FeCo@MN*x*/C (Fig. S4(b) in the ESM) and FeCo@CoN*x*@FeP*x*/C (Fig. S4(c) in the ESM) respectively, indicating the successful fabrication of the metal nitrides and phosphides on the graphited carbon substrates. Note that some Fe_3O_4 was found in FeCo@CoN*x*@FeP*x*/C, which likely came from oxygen in NaH_2PO_4.

More morphology information is further provided by the Raman spectroscopy and BET analysis. Figure 1(g) shows the

Raman spectra of the three samples where the G and D peaks reflect the degree of graphitization and defect structure of the sample, and the characteristic 2D peak of graphene is also observed [42, 43]. For the FeCo/C, the high 2D peak and the small I_{2G}/I_D (less than 1) indicate that graphene multilayers have been formed on the surface of the electrocatalyst, which is consistent with the observations in the TEM images. The graphited carbon substrate could significantly enhance the stability and conductivity of the electrocatalyst. The I_D/I_G of 1.4 indicates the defect-rich structure of the graphited carbon substrate, which would further benefit for the electron transfer in electrocatalysis (Fig. 1(g)). The I_D/I_G value of FeCo@MN*x*/C and FeCo@CoN*x*@FeP*x*/C increases up to 2.2 and 2.9 respectively, significantly higher than that of FeCo/C (Fig. 1(g)). The increased defects of carbon substrate demonstrate that during the NH_3 and PH_3 vapor deposition, the metal nitrides and metal phosphides were successfully constructed. Particularly, the Raman spectrum of FeCo@CoN*x*@FeP*x*/C shows characteristic peaks of respiratory mode at ~ 205 and ~ 305 cm^{-1}, indicating the formation of single wall CNTs. All these observations agree well with the above results from TEM and XRD. BET analysis of FeCo/C, FeCo@MN*x*/C, and FeCo@CoN*x*@FeP*x*/C was performed and their specific surface areas were 105, 137, and 215 $m^2 \cdot g^{-1}$, respectively (Fig. S5(a) in the ESM). In addition, it is shown that micropores dominate in the FeCo/C whilst the FeCo@MN*x*/C and FeCo@CoN*x*@FeP*x*/C especially exhibit high mesoporous contents instead (Fig. 1(h) and Table S1 in the ESM). Particularly for the FeCo@CoN*x*@FeP*x*/C, significantly high content of macroporous structure is observed, as shown in Figs. S5(b) and S5(c) in the ESM. This is due to the staggered arrangement of CNTs on the surface of carbon fibers. It has been reported that the abundant mesopores and macropores are beneficial to the mass transport in electrocatalysis [44].

X-ray photoelectron spectroscopy (XPS) was performed to investigate the surface elemental composition of the FeCo/C, FeCo@MN*x*/C, and FeCo@CoN*x*@FeP*x*/C electrocatalysts. Figure 2 shows the XPS spectra of N 1s, O 1s, Fe 2p, and Co 2p. It is seen from Fig. 2(a) that all three catalysts exhibit the N 1s peaks of graphitic-N at ~ 401 ± 0.1 eV and pyridinic-N at ~ 398.65 ± 0.15 eV and M–N at ~ 399.7 eV [8, 45]. The high content of graphitic-N secures the good conductivity of carbon support. After the CVD of nitrogen, FeCo@MN*x*/C catalysts show characteristic peaks of M–N and the increased content of pyridinic-N, both of which are active sites for ORR and likely come from DMF and/or the annealing treatment with gaseous ammonia. Further CVD with PH_3 reduces the content of pyridinic-N since some of the latter was transformed to phosphide which is also active towards ORR [46, 47]. Figure 2(b) shows that the content of each nitrogen species in the three samples. The total N content increases after N doping while decreases after P deposition, and is 4.2%, 6.2%, and 2.2% respectively. This evidences the successful nitridation and the next substitution of P to partial N.

The high-resolution XPS spectrum of O 1s is shown in Fig. 2(c). The typical peaks are associated with C–O at ~ 533.6 eV, M–OH/MOOH at ~ 531.2 eV, and M–O at ~ 530.3 eV [48]. It is found that the peak of M–OH/MOOH shifted to higher binging energy after nitrogen deposition and then shifted back when phosphides formed. The slightly higher binding energy of FeCo@MN*x*/C at 532.68 eV is likely attributed to the physical or chemical adsorbed water [49]. Given the dominant role of MOH/MOOH in electrocatalysing OER, the different activity of these three samples is ascribed to the content of MOH/MOOH, which is 48.1%, 24.8%, and 43.6% for FeCo/C, FeCo@MN*x*/C, and FeCo@MN*x*@FeP*x*/C respectively (Fig. 2(d)). Therefore, as shown in Fig. 4, the OER activity of FeCo/C and FeCo@CoN*x*@FeP*x*/C is higher than FeCo@MN*x*/C.

Due to the relatively low content of Fe and Co in the samples, the spectra of Fe 2p and Co 2p are slightly noisy. In Figs. 2(e) and 2(f) the peaks of intermetallic bonding and the main peak of MOH/MOOH can be observed. The higher content of MOH/MOOH in the FeCo@CoN*x*@FeP*x*/C catalyst is further demonstrated in the Fe 2p and Co 2p spectra. Note that the Fe–P peak is likely covered by the signal of Fe–OH/OOH. Figure S6 in the ESM shows the C 1s spectra where the satellite peak at around 288.5 eV indicates the graphitization of carbon in all three samples and the peak at about 286 eV is assigned to the C–N/P bonds [41].

To further illustrate the construction process of multiple active components on highly defective and graphitized carbon fiber substrates, X-ray absorption near edge structure (XANES) spectra

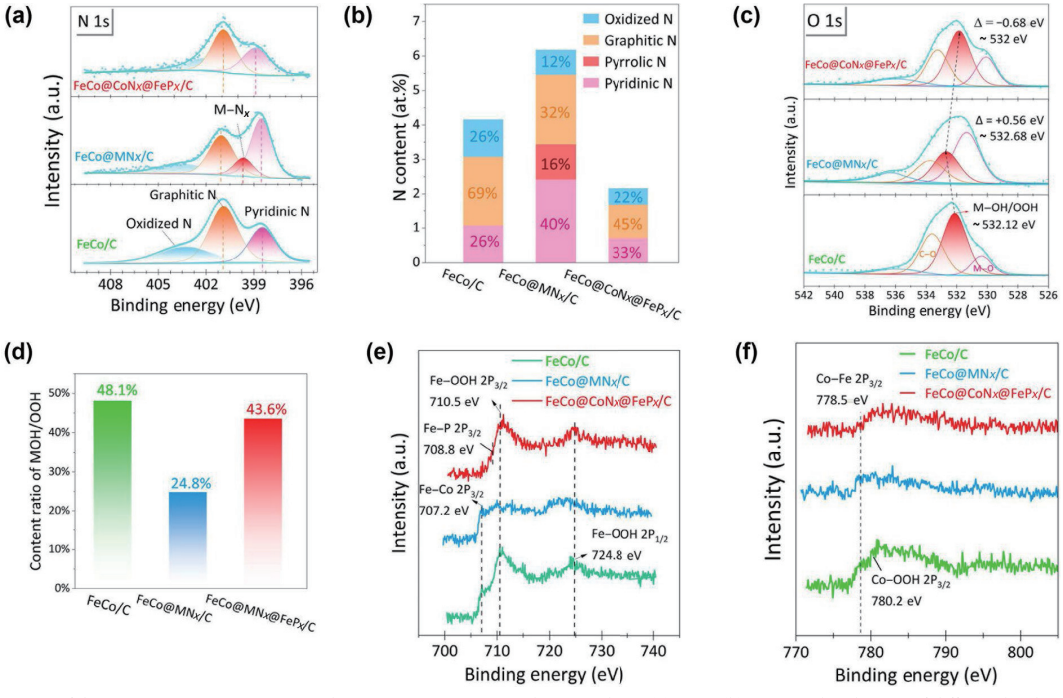

Figure 2 XPS spectra of the FeCo/C, FeCo@MN*x*/C, and FeCo@CoN*x*@FeP*x*/C electrocatalysts: (a) N 1s, (b) content distribution of different kinds of nitrogen, (c) O 1s, (d) content of M–OH/MOOH in the three catalysts, (e) Fe 2p, and (f) Co 2p.

were conducted to investigate the electronic structure of the metal compounds. Figures 3(a) and 3(b) separately show the Fe K-edge and Co K-edge XANES spectra of the FeCo@CoN*x*@FeP*x*/C and their reference samples. Their first derivative curves are shown in the inset. It is found that the Fe K-edge first derivative peak of FeCo@CoN*x*@FeP*x*/C is relatively board and located between FePc and Fe foil, indicating that the main Fe species in FeCo@CoN*x*@FeP*x*/C carry partial positive charges and likely include both metallic Fe and Fe–N/P. The pre-peak at 7,113.5 eV in the Fe K-edge curve of FeCo@CoN*x*@FeP*x*/C is ascribed to its characteristic 1s → $4p_z$ transition, indicating the coordination between Fe and heteroatoms [50, 51]. The Co K-edge first derivative profile shows similar results. The corresponding Fourier transforms (*r*-space) of the extended X-ray-absorption fine structure (FT-EXAFS) data are shown in Figs. 3(d) and 3(e). A prominent peak at ~ 2.3 Å is observed for both Fe and Co, which is close to the spectra of Fe foil and Co foil and ascribed to the scattering path of crystalline phases of Fe–Fe/Co and Co–Co/Fe. From the Fourier transforms of Fe K-edge data, a clear shoulder peak at 1.8 Å is observed, which is attributed to the Fe–P according to the coordination geometry study with the least square fitting analysis. As shown in Fig. 3(c) and Fig. S7 in the ESM, the FeCo@CoN*x*@FeP*x*/C exhibits the best fitting in the both *K* and *R* spaces when Fe–P, Fe–Fe, and Fe–Co contributions are all considered on the first shell of the Fe K-edge. The fitting parameters are list in Table S2 in the ESM. Therefore, it is demonstrated that the shoulder peak at 1.8 Å in the Fe K-edge FT-EXAFS spectrum of FeCo@CoN*x*@FeP*x*/C originates from the Fe–P. Regarding the Co K-edge FT-EXAFS spectra, the shoulder peak at 1.5 Å is similar with that of CoPc and hence attributed to Co–N. The least square fitting analysis further confirms the contribution of Co–N since the combination of Co–N, Co–Fe, and Co–Co on the first shell gives the best fitting result (Fig. S7 and Table S2 in the ESM). The presence of Fe–P and Co–N in FeCo@CoN*x*@FeP*x*/C by XAS indicates that most of the Fe–N pyridine may be converted to Fe–P after doping with PH_3 vapor, and M–N mainly exists in the form of Co–N.

Wavelet transforms-X-ray absorption fine structure (WT-EXAFS) analysis was further conducted to investigate the coordination environment since with this method resolution in both *R*-space and *K*-space can be greatly improved [52, 53]. Figures S8(a) and S8(b) in the ESM show the WT diagram of Fe K-edge and Co K-edge and their extracted contour plots are presented in two forms. From the raw contour plots of the Co K-edge spectra in Fig. S8(c) in the ESM, it is observed that there are three intensity maximums on the first shell, which likely results from the scattering path of Co–N, Fe, and Co [54]. In comparison, only one intensity maximum appears in the contour map of Fe K-edge, which is probably because of the superposition of the P-Fe and Fe-Fe/Co (Fig. S8(d) in the ESM). The above analysis reveals that the FeCo@CoN*x*@FeP*x*/C consists of three metal species including Fe–P, Co–N, and Fe–Co, which would play their important roles in oxygen electrocatalysis. It is also demonstrated that multiple active species have been successfully constructed on the defect-rich and porous carbon substrate via such strategy.

For comparison, the XANES, FT-EXAFS, and WT of the FeCo/C were also analyzed, and the results are shown in Fig. S9 in the ESM. Only one main peak is observed in the FT-EXAFS spectra of both Fe and Co K-edges. The least square fitting indicates that the peak is the superposition result of Fe–Fe or Co–Co and Fe–Co on the first shell, which means that only FeCo alloys exist in FeCo/C.

3.2 OER/ORR activities of electrocatalysts

Having characterized the FeCo/C, FeCo@MN*x*/C, and FeCo@CoN*x*@FeP*x*/C samples, their electrocatalysis towards OER and ORR was separately investigated. The OER performance was first evaluated by performing linear sweep voltammetry (LSV) with a three-electrode system in a 1 M KOH electrolyte. Figures 4(a) and 4(b) show the LSV curves of the three electrocatalysts and IrO_2. A small overpotential for the as-prepared FeCo/C (342 mV), FeCo@MN*x*/C (375 mV), and FeCo@CoN*x*@FeP*x*/C (368 mV) at 10 mA·cm^{-2} is obtained, which is 32, 1, and 7 mV lower than the IrO_2 (375 mV). The Tafel analysis in Fig. 4(c) shows that the FeCo/C (49.5 mV·dec^{-1}) exhibits the most efficient electron transfer, while the Tafel slopes of the FeCo@MN*x*/C (83.6 mV·dec^{-1}) and FeCo@CoN*x*@FeP*x*/C (70.1 mV·dec^{-1}) are close to that of IrO_2 (70.8 mV·dec^{-1}). The OER activity order of

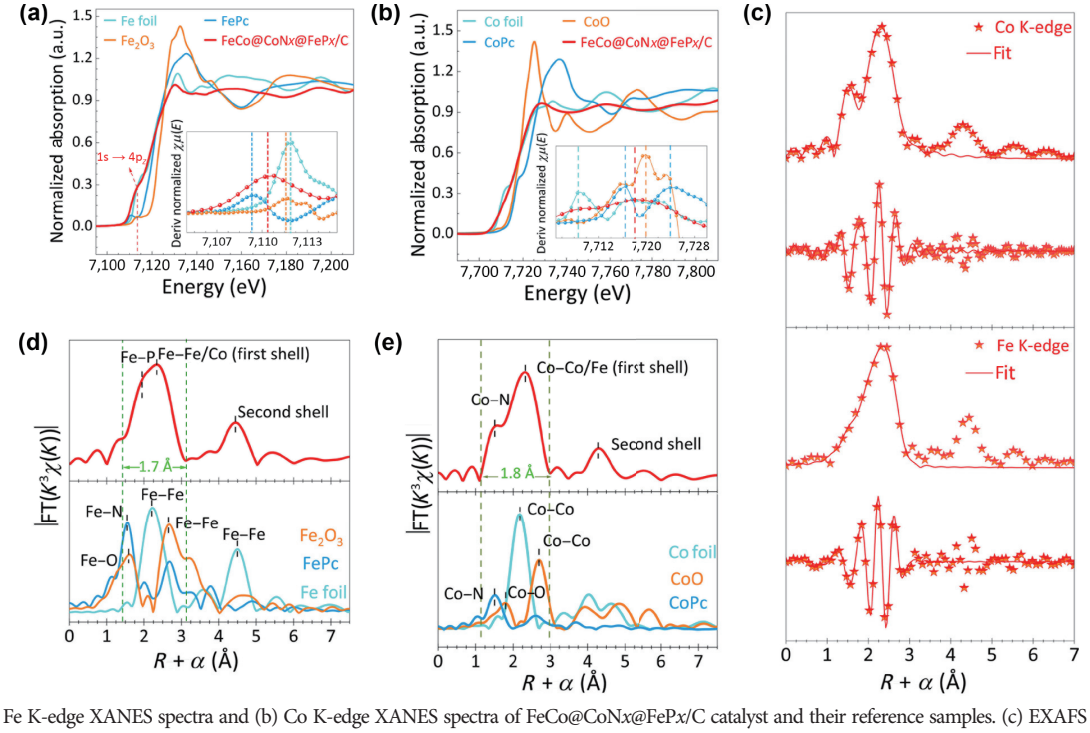

Figure 3 (a) Fe K-edge XANES spectra and (b) Co K-edge XANES spectra of FeCo@CoN*x*@FeP*x*/C catalyst and their reference samples. (c) EXAFS *R*-space fitting curve for FeCo@CoN*x*@FeP*x*/C. The Fourier transform spectra of (d) Fe K-edge spectra and (e) Co K-edge spectra.

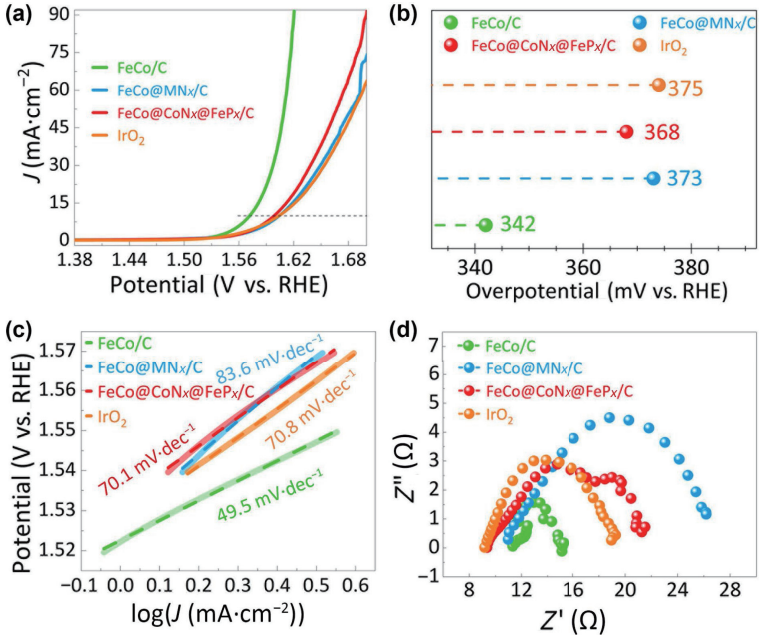

Figure 4 (a) and (b) LSV curves of OER at FeCo/C, FeCo@MN*x*/C, FeCo@CoN*x*@FeP*x*/C, and IrO_2 in N_2-saturated 1 M KOH solution. (c) Tafel plots of OER. (d) EIS curves at 1.75 V vs. reversible hydrogen electrode (RHE).

FeCo/C > FeCo@CoN*x*@FeP*x*/C > FeCo@MN*x*/C is related with the MOH/MOOH active site at these three samples. As discussed in the above XPS analysis, the higher contents of MOH/MOOH at FeCo/C and FeCo@CoN*x*@FeP*x*/C than that of FeCo@MN*x*/C, are likely responsible for the enhanced OER activity of the former two electrocatalysts. In addition to the improvement of intrinsic activity, the porous structure of the carbon fiber constructed by electrospinning and annealing not only accelerates the mass transport but also enhances the electrical conductivity of these electrocatalysts. As shown in the electrochemical impedance spectroscopy (EIS) measurements (Fig. 4(d)), the FeCo/C has the least resistance to charge transfer at the same overpotential, which is consistent with its superior charge transfer activity and smaller Tafel slope. To investigate the working stability of the electrocatalysts, chronoamperometry of the FeCo@CoN*x*@FeP*x*/C and IrO_2 was performed over 10 h and higher current response and stability of the present sample than IrO_2 can be seen (Fig. S10(a) in the ESM). The good stability of the FeCo@CoN*x*@FeP*x*/C is likely due to the coverage of the surface graphene multilayers on the metal active species which were formed in the annealing step. Note that the periodic current fluctuation of the FeCo@CoN*x*@FeP*x*/C catalyst is caused by the continuous growth and release of oxygen bubbles on the catalyst surface [55]. Figure S10(b) and Table S3 in the ESM summarize the OER performance of the electrocatalysts in recent reports. It can be found that the as-prepared three FeCo based electrocatalysts exhibit efficient OER superior to most of carbon-supported FeCo electrocatalysts reported to date.

The electrocatalytic ability of the FeCo/C, FeCo@MN*x*/C, FeCo@CoN*x*@FeP*x*/C, and Pt/C towards ORR was further evaluated via LSV measurement at the scan rate of 10 mV·s^{-1} and rotating speed of 1,600 rap·min^{-1}. As shown in Figs. 5(a) and 5(b), the FeCo/C without CVD treatment behaves less efficient ($E_{1/2}$ = 0.80 V) for ORR than the commercial Pt/C ($E_{1/2}$ = 0.83 V), whilst after doping with nitrogen via CVD the ORR activity of the FeCo@MN*x*/C ($E_{1/2}$ = 0.83 V) is significantly improved and becomes comparable to the Pt/C. Comparing with FeCo/C, FeCo@MN*x*/C, and Pt/C, the FeCo@CoN*x*@FeP*x*/C exhibits the best ORR performance with the highest halfwave potential $E_{1/2}$ of 0.86 V and the smallest Tafel slope of 98 mV·dec^{-1}, as shown in Fig. 5(c). The enhanced ORR activity after CVD of phosphorus further confirms the construction of FeP*x*/CNTs plays a key role in the oxygen electrocatalysis.

In addition, by using rotating disk electrode system, the number of electron transfer for FeCo@CoN*x*@FeP*x*/C was determined to be 3.68–3.74 within 0.1–0.6 V (Fig. 5(d)), which indicates the four-electron transfer of ORR on FeCo@CoN*x*@FeP*x*/C. This is consistent with the result of the variable rotating speed study in LSV (Fig. 5(e)). At the same time, the yield of H_2O_2 is much lower than that of Pt/C. More importantly, the FeCo@CoN*x*@FeP*x*/C electrocatalyst also exhibits outstanding stability with only 3% and 6% decay of its current density after 10 and 20 h of chronoamperometry test, while that of the Pt/C decayed 26% in 10 h (Fig. 5(f)). As shown in Fig. 5(g) and Table S4 in the ESM, the FeCo@CoN*x*@FeP*x*/C exhibits outstanding ORR performance superior to most of the carbon supported FeCo electrocatalysts.

The importance of constructing strategy of the metal compound active species on their electrocatalytic ability was evidenced by conducting the comparison experiments (Fig. S11 in the ESM). Finally, the bifunctional performance of the FeCo@CoN*x*@FeP*x*/C in oxygen electrocatalysis was evaluated and the results are shown in Fig. 5(h) and Table S5 in the ESM. It is found that the present FeCo@CoN*x*@FeP*x*/C ranks top of the reported FeCo based electrocatalysts. Note that the content of metals in FeCo@CoN*x*@FeP*x*/C was determined to be only 3.77 wt.% (2.74 wt.% of Fe and 1.03 wt.% of Co, Table S6 in the ESM) by ICP-OES, demonstrating that the proposed strategy for progressively constructing active species on defect-rich and porous carbon substrate enables the development of highly efficient and stable bifunctional oxygen electrocatalysts.

3.3 Rechargeable zinc-air battery performance

To demonstrate potential applications of the FeCo@CoN*x*@FeP*x*/C sample in practical energy devices, we separately constructed rechargeable ZAB with the FeCo@CoN*x*@FeP*x*/C and commercial Pt/C-IrO_2 loaded carbon cloth as air cathode electrocatalysts. 6.0 M KOH and 0.2 M $Zn(OAc)_2$ aqueous solutions were used as electrolytes, and Zn sheets as anodes (Fig. 6(a)). Figure 6(b) shows that the maximum power density of FeCo@CoN*x*@FeP*x*/C-based ZAB reaches 110 mW·cm^{-2}, which is higher than Pt/C-IrO_2 (104 mW·cm^{-2}) and

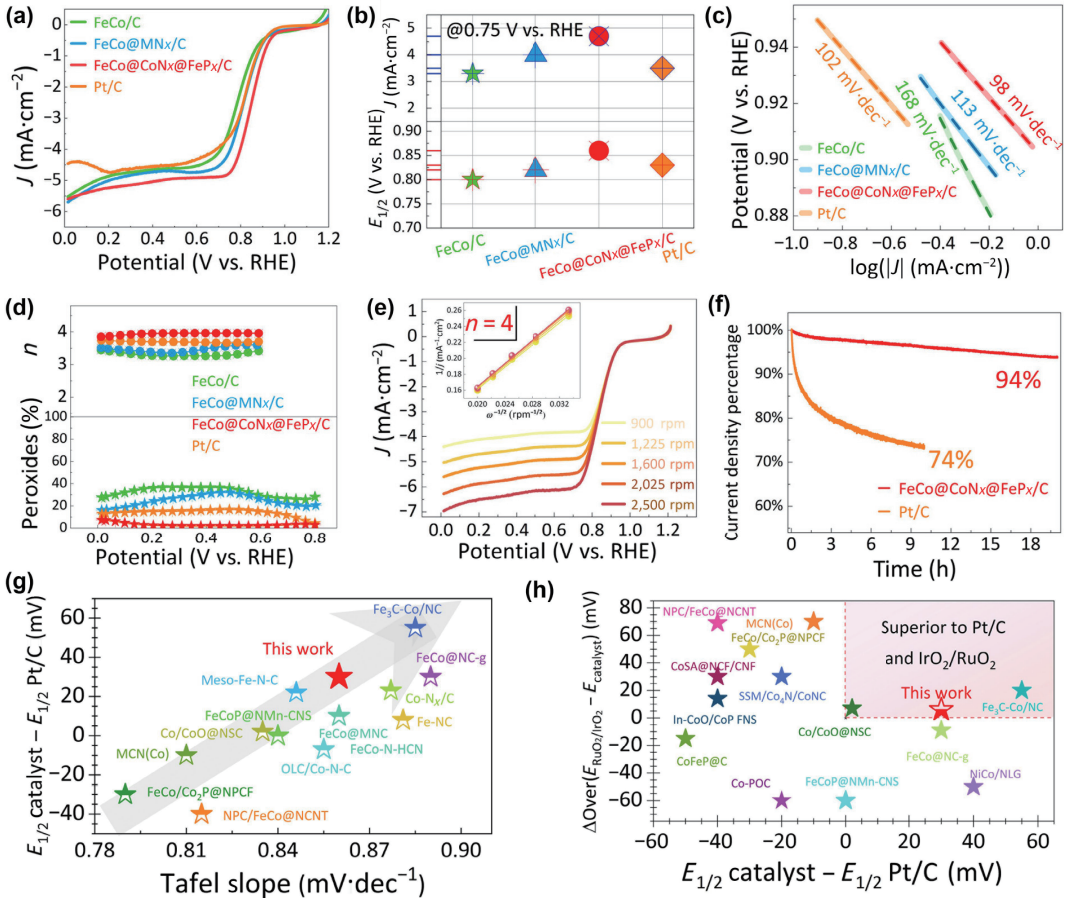

Figure 5 (a) LSV curves of ORR in O_2-saturated 0.1 M KOH solution. (b) Half-wave potential $E_{1/2}$ of different electrocatalysts and limiting current density (J_k) at 0.75 V vs. RHE. (c) Tafel plots of ORR. (d) Number of electron transfer and H_2O_2 yield. (e) LSV and koutecky–levich (k^{-1}) curves of FeCo@CoN*x*@FeP*x*/C catalyst at different rotating speed. (f) Current–time curves of FeCo@CoN*x*@FeP*x*/C and Pt/C at 0.5 V vs. RHE. (g) Comparison of ORR performance with literature. (h) Comparison of ORR/OER performance with literature.

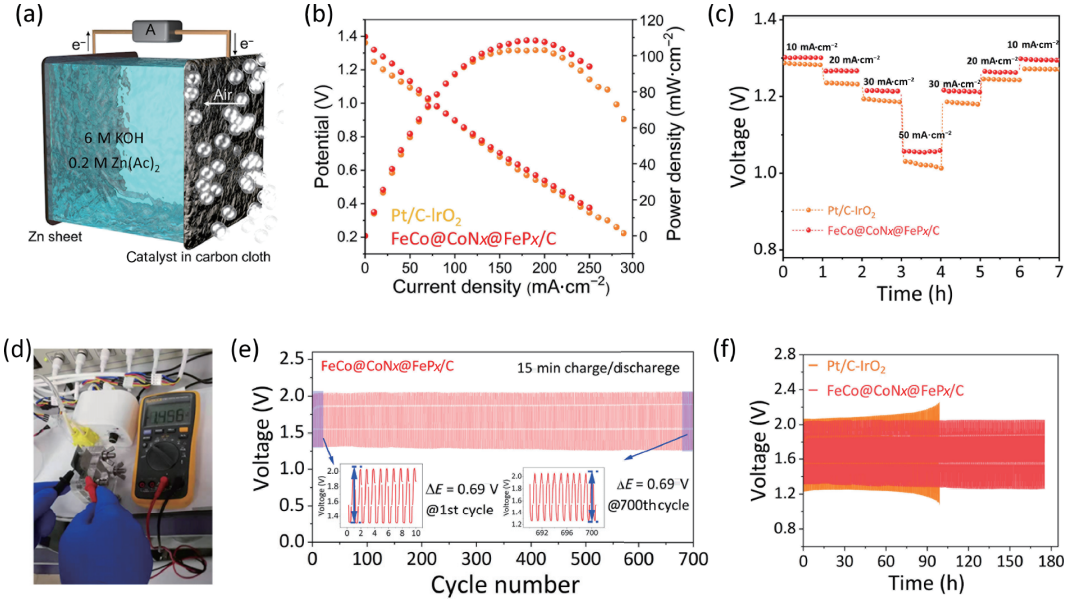

Figure 6 (a) Schematic of rechargeable Zn-air battery configuration. (b) Polarization curves and specific power density curves. (c) Rate performance, discharge voltage at different current densities. (d) Photograph of all-solid-state ZAB displaying a measured open-circuit voltage of 1.456 V. (e) Cyclic stability of FeCo@CoN*x*@FeP*x*/C-based ZAB at 20 mA·cm^{-2}. Insets show the initial charging/discharging curves and those after long-time cycling test. (f) Charge/discharge cycling of a rechargeable ZAB based on FeCo@CoN*x*@FeP*x*/C and Pt/C-IrO_2 at 20 mA·cm^{-2}.

most non-precious metal electrocatalysts [56]. More importantly, the corresponding specific mass power density is as high as 11.7 W·mg_M^{-1} (Fig. S12 in the ESM). In addition, a constant current discharge test (Fig. 6(c)) under different current densities of 10–50 mA·cm^{-2} was carried out and FeCo@CoN*x*@FeP*x*/C exhibited high discharge voltage at each current density, suggesting good high-rate performance. The high open circuit potential of the ZAB is obtained as 1.456 V (Fig. 6(d)), higher than most non-precious metal electrocatalysts [57, 58]. Furthermore, the assembled ZAB showed a low voltage gap (ΔE) of 0.69 V at

20 mA·cm^{-2} corresponding to a round-trip efficiency ($E_{discharge}/E_{charge}$) of 65% and stabilized for 700 charge–discharge cycles (Fig. 6(e)). This high energy efficiency far exceeds most of the Zn-air batteries studied so far [7]. At the same time, the FeCo@CoN*x*@FeP*x*/C-based ZAB was repeatedly cycled at 20 mA·cm^{-2} and stabilized for a total of 175 h (Fig. 6(f)), while the battery with Pt/C-IrO_2-based ZAB underwent gradual degeneration within 90 h. It is hence demonstrated that the FeCo@CoN*x*@FeP*x*/C catalyst assembled Zn-air batteries have superior efficiency and cycling stability than that of Pt/C-IrO_2 noble metal catalyst and most non-precious metal electrocatalysts (Table S7 in the ESM).

4 Conclusions

In summary, the electrospinning technique and CVD method were combined to prepare bifunctional oxygen electrocatalysts by constructing multiple active species on the high-defect and porous graphited carbon fiber substrate. The FeCo nanoparticles with high content of MOH/MOOH active sites for OER on the porous carbon fiber were constructed by the initial electrospinning and annealing treatment. The next CVD of nitrogen leads to the formation of MN*x* in carbon matrix, which boosts the ORR activity. Further phosphatization under PH_3 flow produces the FeP*x* nanoparticles embedded in carbon nanotubes which further improves the bifunctionality of the electrocatalyst. Meanwhile, the graphited CNTs/carbon fiber hierarchical architecture not only stabilized the active centers and increased the conductivity but also significantly maximized the exposure of the active center and boosted the mass transport. As a result, the constructed FeCo@CoN*x*@FeP*x*/C exhibited superior bifunctional electrocatalytic activity and stability to the commercial Pt/C in ORR and IrO_2 in OER. Besides, the FeCo@CoN*x*@FeP*x*/C assembled ZAB showed a high open circuit voltage, large power density, and excellent cycling stability. This work provides pivotal implications on designing advanced bifunctional electrocatalyst for developing high-performance clean energy facilities.

Acknowledgements

The authors acknowledge the grants from the National Natural Science Foundation of China (No. 22004085) and Regional Joint Fund of Guangdong Province (No. 2019A1515111054). The authors also thank the Instrumental Analysis Center of Shenzhen University for the scanning electron microscopy (SEM) and TEM characterizations. The authors would like to thank Yaping Li for Shiyanjia Lab (www.shiyanjia.com) for the XAS analysis.

Electronic Supplementary Material: Supplementary material (XAS data analysis, electrochemical measurement, and electrochemical measurements for liquid ZAB and SEM imaging) is available in the online version of this article at https://doi.org/10.1007/s12274-022-5261-y.

References

[1] Xia, Q.; Zhai, Y. J.; Zhao, L. L.; Wang, J.; Li, D. Y.; Zhang, L. L.; Zhang, J. T. Carbon-supported single-atom catalysts for advanced rechargeable metal-air batteries. *Energy Mater.* **2022**, *2*, 200015.

[2] Pan, L.; Chen, D. F.; Pei, P. C.; Huang, S. W.; Ren, P.; Song, X. A novel structural design of air cathodes expanding three-phase reaction interfaces for zinc-air batteries. *Appl. Energy* **2021**, *290*, 116777.

[3] Yin, Z. Y.; He, R.; Xue, H. B.; Chen, J. J.; Wang, Y.; Ye, X. X.; Xu, N. N.; Qiao, J. L.; Huang, H. T. A bimetallic-activated MnO_2 self-assembly electrode with a dual heterojunction structure for high-performance rechargeable zinc-air batteries. *Energy Mater.* **2022**, *2*, 200021.

[4] Shi, Q.; Liu, Q.; Ma, Y.; Fang, Z.; Liang, Z.; Shao, G.; Tang, B.; Yang, W. Y.; Qin, L.; Fang, X. S. High-performance trifunctional electrocatalysts based on FeCo/Co_2P hybrid nanoparticles for zinc-air battery and self-powered overall water splitting. *Adv. Energy Mater.* **2020**, *10*, 1903854.

[5] Jiao, L.; Li, J. K.; Richard, L. L.; Sun, Q.; Stracensky, T.; Liu, E. S.; Sougrati, M. T.; Zhao, Z. P.; Yang, F.; Zhong, S. C. et al. Chemical vapour deposition of Fe-N-C oxygen reduction catalysts with full utilization of dense Fe-N_4 sites. *Nat. Mater.* **2021**, *20*, 1385–1391.

[6] Balamurugan, J.; Nguyen, T. T.; Kim, N. H.; Kim, D. H.; Lee, J. H. Novel core-shell CuMo-oxynitride@N-doped graphene nanohybrid as multifunctional catalysts for rechargeable zinc-air batteries and water splitting. *Nano Energy* **2021**, *85*, 105987.

[7] Wu, M. J.; Wei, Q. L.; Zhang, G. X.; Qiao, J. L.; Wu, M. X.; Zhang, J. H.; Gong, Q. J.; Sun, S. H. Fe/Co double hydroxide/oxide nanoparticles on N-doped CNTs as highly efficient electrocatalyst for rechargeable liquid and quasi-solid-state zinc-air batteries. *Adv. Energy Mater.* **2018**, *8*, 1801836.

[8] Chen, D. F.; Pan, L.; Pei, P. C.; Song, X.; Ren, P.; Zhang, L. Cobalt-based oxygen electrocatalysts for zinc-air batteries: Recent progress, challenges, and perspectives. *Nano Res.* **2022**, *15*, 5038–5063.

[9] Zhou, X. W.; Liu, X.; Zhang, J. H.; Zhang, C.; Yoo, S. J.; Kim, J. G.; Chu, X. Y.; Song, C.; Wang, P.; Zhao, Z. Z. et al. Highly-dispersed cobalt clusters decorated onto nitrogen-doped carbon nanotubes as multifunctional electrocatalysts for OER, HER and ORR. *Carbon* **2020**, *166*, 284–290.

[10] Zhang, L.; Zhu, J. W.; Li, X.; Mu, S. C.; Verpoort, F.; Xue, J. M.; Kou, Z. K.; Wang, J. Nurturing the marriages of single atoms with atomic clusters and nanoparticles for better heterogeneous electrocatalysis. *Interdiscip. Mater.* **2022**, *1*, 51–87.

[11] Fu, X. G.; Liu, Y. R.; Cao, X. P.; Jin, J. T.; Liu, Q.; Zhang, J. Y. FeCo-N_x embedded graphene as high performance catalysts for oxygen reduction reaction. *Appl. Catal. B* **2013**, *130–131*, 143–151.

[12] Zhao, Y. X.; Lai, Q. X.; Wang, Y.; Zhu, J. J.; Liang, Y. Y. Interconnected hierarchically porous Fe, N-codoped carbon nanofibers as efficient oxygen reduction catalysts for Zn-air batteries. *ACS Appl. Mater. Interfaces* **2017**, *9*, 16178–16186.

[13] Zhou, Q. X.; Hou, S. Y.; Cheng, Y. X.; Sun, R. X.; Shen, W. Y.; Tian, R.; Yang, J.; Pang, H.; Xu, L.; Huang, K. et al. Interfacial engineering Co and MnO within N, S co-doped carbon hierarchical branched superstructures toward high-efficiency electrocatalytic oxygen reduction for robust Zn-air batteries. *Appl. Catal. B* **2021**, *295*, 120281.

[14] Xie, W. W.; Huang, J. H.; Huang, L. T.; Geng, S. P.; Song, S. Q.; Tsiakaras, P.; Wang, Y. Novel fluorine-doped cobalt molybdate nanosheets with enriched oxygen-vacancies for improved oxygen evolution reaction activity. *Appl. Catal. B* **2022**, *303*, 120871.

[15] Xu, H.; Wang, D.; Yang, P. X.; Du, L.; Lu, X. Y.; Li, R. P.; Liu, L. L.; Zhang, J. Q.; An, M. Z. A hierarchically porous Fe-N-C synthesized by dual melt-salt-mediated template as advanced electrocatalyst for efficient oxygen reduction in zinc-air battery. *Appl. Catal. B* **2022**, *305*, 121040.

[16] Lv, X. W.; Xu, W. S.; Tian, W. W.; Wang, H. Y.; Yuan, Z. Y. Activity promotion of core and shell in multifunctional core-shell Co_2P@NC electrocatalyst by secondary metal doping for water electrolysis and Zn-air batteries. *Small* **2021**, *17*, 2101856.

[17] Jin, H. H.; Zhou, H.; He, D. P.; Wang, Z. H.; Wu, Q. L.; Liang, Q. R.; Liu, S. L.; Mu, S. C. MOF-derived 3D Fe-N-S co-doped carbon matrix/nanotube nanocomposites with advanced oxygen reduction activity and stability in both acidic and alkaline media. *Appl. Catal. B* **2019**, *250*, 143–149.

[18] Yang, X. K.; Yi, Q. F.; Sheng, K.; Wang, T. CoNi loaded C–N tubular nanocomposites as excellent cathodic catalysts of alkaline Zn-air batteries. *Catal. Lett.* **2020**, *150*, 2886–2899.

[19] Wan, W. J.; Liu, X. J.; Li, H. Y.; Peng, X. Y.; Xi, D. S.; Luo, J. 3D carbon framework-supported CoNi nanoparticles as bifunctional oxygen electrocatalyst for rechargeable Zn-air batteries. *Appl. Catal. B* **2019**, *240*, 193–200.

[20] Cui, J.; Leng, Y. M.; Xiang, Z. H. FeNi co-doped electrocatalyst synthesized via binary ligand strategy as a bifunctional catalyst for Zn-air flow battery. *Chem. Eng. Sci.* **2022**, *247*, 117038.
[21] Shi, X. J.; He, B. B.; Zhao, L.; Gong, Y. S.; Wang, R.; Wang, H. W. FeS_2-CoS_2 incorporated into nitrogen-doped carbon nanofibers to boost oxygen electrocatalysis for durable rechargeable Zn-air batteries. *J. Power Sources* **2021**, *482*, 228955.
[22] Zhang, C. L.; Liu, J. T.; Li, H.; Qin, L.; Cao, F. H.; Zhang, W. The controlled synthesis of Fe_3C/Co/N-doped hierarchically structured carbon nanotubes for enhanced electrocatalysis. *Appl. Catal. B* **2020**, *261*, 118224.
[23] Gao, L.; Chang, S. M.; Zhang, Z. Y. High-Quality CoFeP Nanocrystal/N, P dual-doped carbon composite as a novel bifunctional electrocatalyst for rechargeable Zn-air battery. *ACS Appl. Mater. Interfaces* **2021**, *13*, 22282–22291.
[24] Zhang, X. L.; Yang, Z. X.; Lu, Z. S.; Wang, W. C. Bifunctional CoN_x embedded graphene electrocatalysts for OER and ORR: A theoretical evaluation. *Carbon* **2018**, *130*, 112–119.
[25] Zhang, Y. Y.; Sun, H. H.; Qiu, Y. F.; Ji, X. Y.; Ma, T. G.; Gao, F.; Ma, Z.; Zhang, B. X.; Hu, P. A. Multiwall carbon nanotube encapsulated Co grown on vertically oriented graphene modified carbon cloth as bifunctional electrocatalysts for solid-state Zn-air battery. *Carbon* **2019**, *144*, 370–381.
[26] Li, R. Z.; Wang, D. S. Understanding the structure-performance relationship of active sites at atomic scale. *Nano Res.* **2022**, *15*, 6888–6923.
[27] Ibraheem, S.; Li, X. T.; Shah, S. S. A.; Najam, T.; Yasin, G.; Iqbal, R.; Hussain, S.; Ding, W. Y.; Shahzad, F. Tellurium triggered formation of Te/Fe-NiOOH nanocubes as an efficient bifunctional electrocatalyst for overall water splitting. *ACS Appl. Mater. Interfaces* **2021**, *13*, 10972–10978.
[28] Chen, D. F.; Pan, L.; Pei, P. C.; Huang, S. W.; Ren, P.; Song, X. Carbon-coated oxygen vacancies-rich Co_3O_4 nanoarrays grow on nickel foam as efficient bifunctional electrocatalysts for rechargeable zinc-air batteries. *Energy* **2021**, *224*, 120142.
[29] Yan, L.; Xu, Z. Y.; Hu, W. K.; Ning, J. Q.; Zhong, Y. J.; Hu, Y. Formation of sandwiched leaf-like CNTs-Co/$ZnCo_2O_4$@NC-CNTs nanohybrids for high-power-density rechargeable Zn-air batteries. *Nano Energy* **2021**, *82*, 105710.
[30] Shi, Q.; Liu, Q.; Zheng, Y. P.; Dong, Y. Q.; Wang, L.; Liu, H. T.; Yang, W. Y. Controllable construction of bifunctional Co_xP@N,P-doped carbon electrocatalysts for rechargeable zinc-air batteries. *Energy Environ. Mater.* **2022**, *5*, 515–523.
[31] Liu, Y. F.; Li, Y.; Wu, Q.; Su, Z.; Wang, B.; Chen, Y. F.; Wang, S. F. Hollow CoP/FeP_4 heterostructural nanorods interwoven by CNT as a highly efficient electrocatalyst for oxygen evolution reactions. *Nanomaterials* **2021**, *11*, 1450.
[32] Hu, Q.; Wang, Z. Y.; Huang, X. W.; Qin, Y. J.; Yang, H. P.; Ren, X. Z.; Zhang, Q. L.; Liu, J. H.; He, C. X. A unique space confined strategy to construct defective metal oxides within porous nanofibers for electrocatalysis. *Energy Environ. Sci.* **2020**, *13*, 5097–5103.
[33] Wang, Y. Y.; Li, Z. G.; Zhang, P.; Pan, Y.; Zhang, Y.; Cai, Q.; Silva, S. R. P.; Liu, J.; Zhang, G. X.; Sun, X. M. et al. F. Flexible carbon nanofiber film with diatomic Fe-Co sites for efficient oxygen reduction and evolution reactions in wearable zinc-air batteries. *Nano Energy* **2021**, *87*, 106147.
[34] Li, C. L.; Zhang, Z. J.; Wu, M. C.; Liu, R. FeCoNi ternary alloy embedded mesoporous carbon nanofiber: An efficient oxygen evolution catalyst for rechargeable zinc-air battery. *Mater. Lett.* **2019**, *238*, 138–142.
[35] Yu, H.; Zhang, D. D.; Hou, H. L.; Ma, Y.; Fang, Z.; Lu, X. L.; Xu, S.; Hou, P.; Shao, G.; Yang, W. Y. et al. Embedded FeCo alloy nanoparticles in N-doped mesoporous carbon nanofibers as efficient bi-functional electrocatalysts for long-term rechargeable Zn-air batteries. *Appl. Surf. Sci.* **2022**, *571*, 151292.
[36] Yazici, M. S.; Azder, M. A.; Salihoglu, O. CVD grown graphene as catalyst for acid electrolytes. *Int. J. Hydrogen Energy* **2018**, *43*, 10710–10716.
[37] Konar, R.; Das, S.; Teblum, E.; Modak, A.; Perelshtein, I.; Richter, J. J.; Schechter, A.; Nessim, G. D. Facile and scalable ambient pressure chemical vapor deposition-assisted synthesis of layered silver selenide (β-Ag_2Se) on Ag foil as a possible oxygen reduction catalyst in alkaline medium. *Electrochim. Acta* **2021**, *370*, 137709.
[38] Wu, Y. C.; Wang, Y. J.; Wang, Z. W.; Li, X. T. Highly dispersed CoP on three-dimensional ordered mesoporous FeP for efficient electrocatalytic hydrogen production. *J. Mater. Chem. A.* **2021**, *9*, 23574–23581.
[39] Chen, S. H.; Huang, Y. Q.; Li, M.; Sun, P. P.; Lv, X. W.; Li, B.; Fang, L.; Sun, X. H. MnO_x anchored on N and O Co-doped carbon nanotubes encapsulated with FeCo alloy as highly efficient bifunctional electrocatalyst for rechargeable zinc-air batteries. *J. Electroanal. Chem.* **2021**, *895*, 115513.
[40] Wang, Z.; Ang, J. M.; Zhang, B. W.; Zhang, Y. F.; Ma, X. Y. D.; Yan, T.; Liu, J.; Che, B. Y.; Huang, Y. Z.; Lu, X. H. FeCo/FeCoNi/N-doped carbon nanotubes grafted polyhedron-derived hybrid fibers as bifunctional oxygen electrocatalysts for durable rechargeable zinc-air battery. *Appl. Catal. B* **2019**, *254*, 26–36.
[41] Yang, Z. K.; Zhao, C. M.; Qu, Y. T.; Zhou, H.; Zhou, F. Y.; Wang, J.; Wu, Y. E.; Li, Y. D. Trifunctional self-supporting cobalt-embedded carbon nanotube films for ORR, OER, and HER triggered by solid diffusion from bulk metal. *Adv. Mater.* **2019**, *31*, 1808043.
[42] Yang, X. D.; Zheng, Y. P.; Yang, J.; Shi, W.; Zhong, J. H.; Zhang, C. K.; Zhang, X.; Hong, Y. H.; Peng, X. X.; Zhou, Z. Y. et al. Modeling Fe/N/C catalysts in monolayer graphene. *ACS Catal.* **2017**, *7*, 139–145.
[43] Liang, Z. Z.; Kong, N. N.; Yang, C. X.; Zhang, W.; Zheng, H. Q.; Lin, H. P.; Cao, R. Highly curved nanostructure-coated Co, N-doped carbon materials for oxygen electrocatalysis. *Angew. Chem., Int. Ed.* **2021**, *60*, 12759–12764.
[44] Yu, N. F.; Chen, H.; Kuang, J. B.; Bao, K. L.; Yan, W.; Ye, J. L.; Yang, Z. T.; Huang, Q. H.; Wu, Y. P.; Sun, S. G. Efficient oxygen electrocatalysts with highly-exposed Co-N_4 active sites on N-doped graphene-like hierarchically porous carbon nanosheets enhancing the performance of rechargeable Zn-air batteries. *Nano Res.* **2022**, *15*, 7209–7219.
[45] Tang, C.; Wang, B.; Wang, H. F.; Zhang, Q. Defect engineering toward atomic Co-N_x-C in hierarchical graphene for rechargeable flexible solid Zn-air batteries. *Adv. Mater.* **2017**, *29*, 1703185.
[46] Han, M. N.; Shi, M. J.; Wang, J.; Zhang, M. L.; Yan, C.; Jiang, J. T.; Guo, S. H.; Sun, Z. Y.; Guo, Z. H. Efficient bifunctional Co/N dual-doped carbon electrocatalysts for oxygen reduction and evolution reaction. *Carbon* **2019**, *153*, 575–584.
[47] Zhang, J. T.; Zhang, T.; Ma, J.; Wang, Z.; Liu, J. H.; Gong, X. Z. ORR and OER of Co-N codoped carbon-based electrocatalysts enhanced by boundary layer oxygen molecules transfer. *Carbon* **2021**, *172*, 556–568.
[48] Kim, N. I.; Sa, Y. J.; Yoo, T. S.; Choi, S. R.; Afzal, R. A.; Choi, T.; Seo, Y. S.; Lee, K. S.; Hwang, J. Y.; Choi, W. S. et al. Oxygen-deficient triple perovskites as highly active and durable bifunctional electrocatalysts for oxygen electrode reactions. *Sci Adv.* **2018**, *4*, eaap9360.
[49] Li, M. X.; Zhu, Y.; Wang, H. Y.; Wang, C.; Pinna, N.; Lu, X. F. Ni strongly coupled with Mo_2C encapsulated in nitrogen-doped carbon nanofibers as robust bifunctional catalyst for overall water splitting. *Adv. Energy Mater.* **2019**, *9*, 1803185.
[50] Cao, R. G.; Thapa, R.; Kim, H.; Xu, X. D.; Gyu Kim, M.; Li, Q.; Park, N.; Liu, M. L.; Cho, J. Promotion of oxygen reduction by a bio-inspired tethered iron phthalocyanine carbon nanotube-based catalyst. *Nat. Commun.* **2013**, *4*, 2076.
[51] Li, H. X.; Wen, Y. L.; Jiang, M.; Yao, Y.; Zhou, H. H.; Huang, Z. Y.; Li, J. W.; Jiao, S. Q.; Kuang, Y. F.; Luo, S. L. Understanding of neighboring Fe-N_4-C and Co-N_4-C dual active centers for oxygen reduction reaction. *Adv. Funct. Mater.* **2021**, *31*, 2011289.
[52] Zhou, K. L.; Wang, Z. L.; Han, C. B.; Ke, X. X.; Wang, C. H.; Jin, Y. H.; Zhang, Q. Q.; Liu, J. B.; Wang, H.; Yan, H. Platinum single-atom catalyst coupled with transition metal/metal oxide heterostructure for accelerating alkaline hydrogen evolution reaction. *Nat. Commun.* **2021**, *12*, 3783.
[53] Li, J. J.; Jiang, Y. F.; Wang, Q.; Xu, C. Q.; Wu, D. J.; Banis, M. N.;

Adair, K. R.; Doyle-Davis, K.; Meira, D. M.; Finfrock, Y. Z. et al. A general strategy for preparing pyrrolic-N_4 type single-atom catalysts via pre-located isolated atoms. *Nat. Commun.* **2021**, *12*, 6806.

[54] Fei, H. L.; Dong, J. C.; Arellano-Jiménez, M. J.; Ye, G. L.; Dong Kim, N.; Samuel, E. L. G.; Peng, Z. W.; Zhu, Z.; Qin, F.; Bao, J. M. et al. Atomic cobalt on nitrogen-doped graphene for hydrogen generation. *Nat. Commun.* **2015**, *6*, 8668.

[55] Tiwari, J. N.; Sultan, S.; Myung, C. W.; Yoon, T.; Li, N. N.; Ha, M. R.; Harzandi, A. M.; Park, H. J.; Kim, D. Y.; Chandrasekaran, S. S. et al. Multicomponent electrocatalyst with ultralow Pt loading and high hydrogen evolution activity. *Nat. Energy* **2018**, *3*, 773–782.

[56] Yan, J. H.; Wang, Y.; Zhang, Y. Y.; Xia, S. H.; Yu, J. Y.; Ding, B. Direct magnetic reinforcement of electrocatalytic ORR/OER with electromagnetic induction of magnetic catalysts. *Adv. Mater.* **2021**, *33*, 2007525.

[57] Wang, T. T.; Liu, M.; Chaemchuen, S.; Wang, J. C.; Yuan, Y.; Chen, C.; Qiao, A.; Verpoort, F.; Kou, Z. K. Constructing a stable cobalt-nitrogen-carbon air cathode from coordinatively unsaturated zeolitic-imidazole frameworks for rechargeable zinc-air batteries. *Nano Res.* **2022**, *15*, 5895–5901.

[58] Yang, G. G.; Zhu, J. W.; Yuan, P. F.; Hu, Y. F.; Qu, G.; Lu, B. A.; Xue, X. Y.; Yin, H. B.; Cheng, W. Z.; Cheng, J. Q. et al. Regulating Fe-spin state by atomically dispersed Mn-N in Fe-N-C catalysts with high oxygen reduction activity. *Nat. Commun.* **2021**, *12*, 1734.